Ultrasonics 93 (2019) 130–138

Contents lists available at ScienceDirect

Ultrasonics

journal homepage: www.elsevier.com/locate/ultras

# Theoretical and experimental investigations of ultrasonic sound fields in thin bubbly liquid layers for ultrasonic cavitation peening

Fushi Bai*, Yangyang Long, Kai-Alexander Saalbach, Jens Twiefel

*Institute of Dynamics and Vibration Research, Leibniz University Hannover, Appelstr. 11, Hannover 30167, Germany*

ARTICLE INFO

*Keywords:*
Ultrasonic cavitation peening
Sonochemiluminescence
Bubbly liquid layer
Standoff distance

ABSTRACT

Ultrasonic cavitation peening is a potential surface enhancement process. During this process a high input power is necessary to obtain an effective process result. A small gap, usually less than 1 mm, between the sonotrode tip and the treated surface is also required to avoid substantial energy loss. Due to the high vibration of the sonotrode, many cavitation bubbles are generated, forming a thin bubbly liquid layer in the small gap. The cavitation bubbles in the layer seriously disturb the sound wave propagation and interact with each other. The disturbances and interactions change the intensity and the spatial distribution of cavitation bubbles, resulting in the different interactions between cavitation bubbles and workpiece surfaces. The variations of the interactions cause different surface properties of the workpieces after ultrasonic cavitation peening. Therefore, quantifying the ultrasound field in different conditions is of great important to improve the ultrasonic cavitation peening process. A current model of the sound propagation in the bubbly liquid was already developed but did not include the bubble interactions. In this work, the bubble interactions are taken into account to improve the current model. The calculated results of the sound field with the improved model are validated by sonochemiluminescence experiments in various standoff distances and vibration amplitudes. Both of the experimental and the calculated results show that the highest sound pressure is generated when the vibration amplitude is around 25 μm. The strongest cavitation intensity occurs at the gap width of 0.5–0.7 mm.

## 1. Introduction

Ultrasonic cavitation peening is a novel metal surface enhancement technology that takes the advantage of the incubation period of metal materials caused by the power ultrasound [1]. It is inexpensive to perform and completed without the obvious increase of the surface roughness. The main part -. a piezoelectric transducer that generates vibrations, has a compact structure and is easy to control [2]. Furthermore, this surface enhancement process is considered as an environmentally friendly technology since no polluting effluents are produced [3].

Several investigations on ultrasonic cavitation peening have been reported in the last decades. Sriraman et al. [5] used a 1.5 mm gap width between the sonotrode tip and the specimen surface to improve the residual stress introduced by ultrasonic cavitation. The gap width is defined as the standoff distance Mathias et al. [4] explored the effects of ultrasonic cavitation on specimen texture at a standoff distance of 0.7 mm. Gao et al. [6] found that the higher vibration amplitude of the sonotrode can increase the surface hardness when the standoff distance is 1 mm. Sasaki et al. [7] utilized the influences of cavitation peening on the treated surface to enhance the fatigue life, keeping the standoff distance at 1 mm. Kim et al. [8] used a standoff distance of approximately 1 mm to investigate the damage behavior of Al alloy by ultrasonic cavitation. They found that the weight loss increases with the increase of vibration amplitude. Bai et al. [9] treated an Al alloy specimen surface utilizing ultrasonic cavitation at a standoff distance of 0.7 mm. It is found that the most significant improvement of microhardness occurs at the end of incubation period. From the sources [5–9] it can be seen that during ultrasonic cavitation peening, a small standoff distance is required, usually less than 1 mm. After the treatment, the surface properties are improved significantly. Thus, the investigations on the cavitation bubbles in thin liquid layers are necessary and important for the ultrasonic cavitation peening process.

The dynamics (growth and collapses) of cavitation bubbles is greatly affected by the standoff distance. When the maximum volume of a cavitation bubble is limited by the standoff distance, the bubble is no longer spherical. Along with the reduction of the standoff distance, the shape of cavitation bubbles at the maximum volume changes from an ellipsoidal shape to a flattened hourglass shape [10]. Correspondingly, the collapse form changes from splitting collapse to neutral collapse

* Corresponding author.
*E-mail addresses:* bai@ids.uni-hannover.de, baifushi@hotmail.com (F. Bai).

https://doi.org/10.1016/j.ultras.2018.11.010
Received 15 August 2018; Received in revised form 26 November 2018; Accepted 26 November 2018
Available online 27 November 2018

[11] When the ratio of the standoff distance to the maximum bubble diameter is larger than 2.2, the cavitation bubble shows a spherical form at the expansion stage [12]. To investigate the bubble structures in a small gap, high-speed photographs were synchronously captured with the sinusoidal wave signal from the vibratory generator while the features of the eroded specimen surfaces were revealed by a scanning electron microscopy [13]. It is found that the dominant cavitation erosion is caused by the shock wave from the collapse of the bubble cluster. To simply and accurately visualize ultrasonic cavitation field, increasing interests has been paid to the use of sonochemiluminescence (SCL) [14]. SCL is a phenomenon emitting light which is produced by the $OH^-$ and the sonochemically oxidized luminol. A blue fluorescence can emit when luminol reacts with the hydroxyl radicals generated by acoustic cavitation [15]. Many researchers [16–18] studied the cavitation field by taking advantage of SCL which can describe the superposition of ultrasound waves. The emission can be recorded and evaluated by photo with a long time exposure [19].

During ultrasonic cavitation peening, the physical effects of ultrasonic cavitation at water-metal interface are utilized to improve the workpiece surface properties. Thus, the cavitation bubbles near the workpiece surfaces significantly affect the process results. The dynamics (growths and collapses) of cavitation bubbles greatly disturb the sound field and the bubble sizes depend on the sound pressure. Apart from the dynamics of bubbles, there are interaction between cavitation bubbles, disturbing sound field as well. The aim of this paper is to provide a theoretical and experimental analysis to evaluate the intensity and distribution of cavitation bubbles at different standoff distances and input power. Although a previous model was developed to evaluate the sound propagation in a bubbly liquid, the bubble interactions was not considered. To more precisely identify the sound distribution, in this paper a combination of the sound propagation model with the bubble interactions and a sound field distribution model is developed. Then, to verify the model, the SCL experiments are carried out to show the mean and local distributions of the cavitation bubbles in the thin bubbly liquid layers.

## 2. Theory

During ultrasonic cavitation peening, a small standoff distance is usually used to avoid undesired energy losses. Even a small change of the standoff distance could have a significant effect on the growth and collapses of cavitation bubbles. Consequently, the results of ultrasonic cavitation peening changes with various standoff distances. The generation of sound waves requires two basic conditions: a wave source and an elastic medium of sound propagation. In order to describe the wave motion, the relationship between the sound pressure, the particle velocity, the changes in density and sound speed has to be established. By neglecting gravity and assuming the ambient fluid velocity to be zero, the ambient pressure is then constant. Based on the previous works [20], the wave motions in an ideal medium can be liberalized as the modified Helmholtz equation, which is shown in Eq. (1).

$$\nabla^2 p + k_m^2 p = 0 \tag{1}$$

where $p$ represents the pressure, $\nabla$ is the gradient operator and $k_m$ is the wavenumber.

When the sound wave propagates in the bubbly liquid, the incident sound wave will be scattered by the small bubbles in the liquid, which leads to a scattering sound field. Besides, the vibrations of the bubbles also radiate sound field to the ambience. Therefore, these phenomena interact with each other when the sound wave propagates in the bubbly liquid.

In the classical linear theory, the average sound speed, density and pressure are used to describe the related physical parameters in the bubbly liquid. For the bubbles in the medium, it is assumed that all the bubbles have the same equilibrium radius and the number of the bubbles is the same in a unit volume. According to the studies by Wijngaarden et al. [21], the complex wavenumber $k_m$ is defined as:

$$k_m^2 = \frac{\omega^2}{c^2} + 4\pi\omega^2 \int_0^\infty \frac{af(a)}{\omega_0^2 - \omega^2 + 2ib\omega} da \tag{2}$$

In this equation, $\omega$ is the frequency of the wave and $c$ is the sound speed in the pure liquid. $\omega_0$ and $b$ are the resonance frequency of bubbles and the damping factor, respectively. $a$ is a bubble radius. The distributions of the bubble radii are considered as a Gaussian distribution $f(a)$ as shown in Eq. (3). It is assumed that the bubble radii ranging from $a_1$ to $a_2$.

$$f(a) = \begin{cases} B\exp[-(a-a_0)^2/\sigma_B^2], & a_1 < a < a_2, \\ 0, \ otherwise \end{cases} \tag{3}$$

$\sigma$ is the standard deviation and $B$ is used as a scaling factor for matching the gas volume fraction. $a_0$ has a value of $(a_1 + a_2)/2$.

Based the classical theory, Fuster et al. [23] took into consideration of the interactions among cavitation bubbles and used Eq. (4) to improve Eq. (2).

$$I_0 = \frac{1}{\rho}\frac{3\beta}{(a\omega/c)^2}\left[1 - \exp\left(-i\frac{2.3a\omega}{c\beta^{1/3}}\right)\left(1 + \frac{i\omega c\beta^{1/3}}{2.3a}\right)\right]\left(p_{ge}\Phi - \frac{2\sigma}{a} + 4\mu i\omega\right) \tag{4}$$

where $I_0$ is the potential from the surrounding bubbles. $P_{ge}$ is the initial gas pressure, which gives mechanical equilibrium under the reference liquid pressure $P_0$. $\Phi$ is a complex function.

$$\Phi = \frac{3\gamma}{1 - 3(\gamma-1)ix[(i/x)^{1/2}\coth(i/x)^{1/2} - 1]} \tag{5}$$

and

$$x = D_f/\omega a^2 \tag{6}$$

where $D_f$ is the gas thermal diffusivity.

Then the modified resonance frequency and the damping coefficient are shown in Eq. (7) and Eq. (8), respectively [23].

$$\omega_0^2 = \frac{p_0}{\rho a}\left(\mathrm{Re}\ \Phi - \frac{2\sigma}{ap_0}\right) + \frac{\mathrm{Re}\, I_0}{a^2} \tag{7}$$

$$b = \frac{2\mu}{\rho a^2} + \frac{p_0}{2\omega\rho a^2}\mathrm{Im}\,\Phi + \frac{\omega^2 a}{2c} + \frac{\mathrm{Im}\, I_0}{2\omega a^2} \tag{8}$$

The complex wave vector $k_m$ contains all of the information needed to calculate the propagation of sound waves in a two phase medium. Thus the speed of the sound wave and the attenuation coefficient is deduced in Eq. (9) and Eq. (10), respectively [22].

$$c_m = \frac{\omega}{\mathrm{Re}(k_m)} \tag{9}$$

$$\alpha_m = \mathrm{Im}(k_m) \tag{10}$$

In the case of a linear relationship of approximately $2 \times 10^{-9}$/Pa between the bubble volume fraction $\beta$ and the acoustic pressure amplitude $p$ [24], the final volume fraction value can be calculated from the Eqs. (1) and (2) [29].

The schematic diagram of a typical ultrasonic cavitation peening system is shown in Fig. 1. In this configuration, cylindrical coordinates ($R_s$, $\theta$, $z$) are used, where $R_s$ is the radius from the center of horn tip, $\theta$ the angle of that radius, and $z$ a length in the direction normal to the specimen surface. The sound field to be considered can be simplified and described as follows: the vibration of the horn tip is piston-like and generates a sound beam in front of it. Then, it is assumed that the radiation surface is a fixed rigid wall at $z = 0$ and the workpiece surface is a rigid wall at $z = L$. The sound wave first travels through the cavitation field in $z$ direction from the radiation surface to the specimen surface in $z$ direction. Then it gets reflected by the specimen surface and

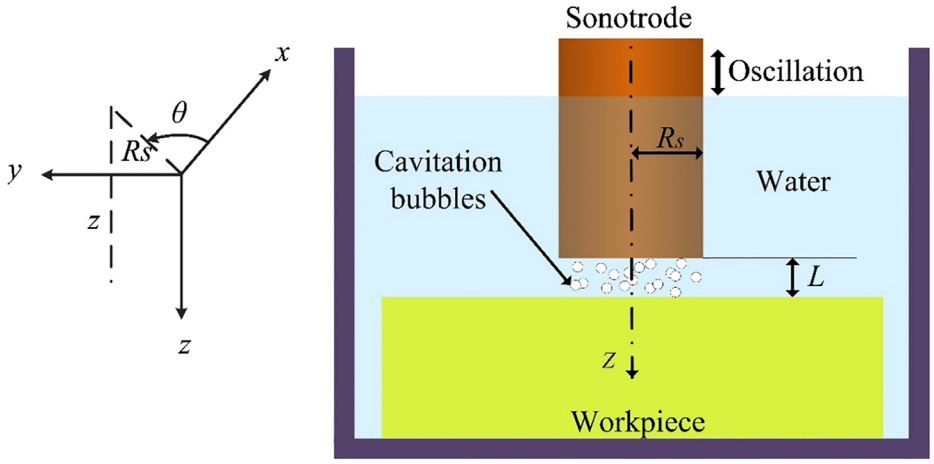


**Fig. 1.** Scheme of the ultrasonic cavitation peening system.

propagates towards the radiation surface again. The reflection of the wave goes on and on in the small gap until the wave totally dissipates in the bubbly liquid. The other surfaces, i.e. water surface, are considered as ideal pressure release boundaries.

In the case shown in Fig. 1, the sound source is a flat disc and vibrates harmonically in $z$ direction. The flat disc reflects and constrains the radiation into the half-space with the entire acoustic energy. The point source is considered as the infinitesimal area $dS'$. The distance from point $M$ to the source is $\mathbf{r'_M}$ while to the center of the flat disc is $\mathbf{r_M}$. Therefore, the total pressure from all the elemental areas is expressed in Eq. (11) in frequency domain if there is no boundary in front of the sonotrode tip [24].

$$p(\mathbf{r_M}) = \frac{i\omega\rho}{2\pi} u_0 \iint_{S'} \frac{e^{i(k_m|\mathbf{r'_M}-\mathbf{r_M}|)}}{|\mathbf{r'_M}-\mathbf{r_M}|} dS' \tag{11}$$

where $u_0$ is the peak amplitude of the transducer velocity. According to [25], the water surface where pressure vanishes can be assumed as an ideal pressure-release boundary. In this work, only the sound field in the gap is calculated. Thus the boundaries excepting the surface of treated specimen are assumed to be ideal pressure release boundaries. Eq. (12) describes this situation.

$$p(\mathbf{r_M}) = 0 \tag{12}$$

Regarding the rigid wall, a vanishing derivative of the pressure normal to the boundary is determined in Eq. (13).

$$\frac{\partial p(\mathbf{r_M})}{\partial \mathbf{n}} = 0 \tag{13}$$

The sound pressure at any point $M$ is obtained from Eq. (11) using the complex wave number $k_m$ with the consideration of bubble interactions. Then, the sound filed without boundary in front of the sonotrode tip is calculated. Since the standoff distance is small in our model, the liquid is considered as a liquid with a homogeneous distribution of cavitation bubbles. The workpiece surface is considered as a rigid wall which is infinite and directly converts the wave propagation direction. As a result, the original sound field is overlaid with the reflection sound filed. The sound pressure is overlapped again and again until the sound pressure tends to zero. Therefore, the acoustic field with the consideration of bubble interactions is simulated by following the above description.

## 3. Simulation of the sound field in bubbly liquid

The sound speed and attenuation coefficient in the bubbly liquid are initially calculated. The parameters that are needed in the simulations are provided in Table 1. As validated by Dähnke et al. [25], the bubble radii ranging from $a_1 = 5\,\mu m$ and $a_2 = 3\,mm$ while the standard deviation $\sigma$ is set to be 2 mm.

**Table 1**
Values of the physical parameters used in the model.

| Physical parameters | Unit | Values |
|---|---|---|
| Density | ρ (kg/m$^3$) | 998.21 |
| Surface tension coefficient | σ (N/m) | 0.07236 |
| coefficient of viscosity | μ (Pa/s) | 0.001 |
| Static pressure | $P_0$ (Pa) | $1.013 \times 10^5$ |
| Vapor pressure | $P_{ge}$ (Pa) | $2.34 \times 10^3$ |
| polytropic exponent | K | 1 |
| Sound speed of the host liquid | c (m/s) | 1500 |
| Ratio of specific heats | γ | 1.4 |
| Gas thermal diffusivity | D (m$^2$/s) | $2.4 \times 10^{-4}$ |

According to Eqs. (9) and (10), the attenuation coefficient and the propagation velocity of sound waves were calculated. Fig. 2(a) shows the changes of the attenuation coefficient with and without the interaction of bubbles. Since the typical volume fraction caused by ultrasonic cavitation liquid is up to 1%, in the calculation the range of the volume fraction is up to 1.7%. It can be seen that the attenuation coefficient increases with increasing the vapor volume fraction. The attenuation generally is generally caused by the scattering, absorption of the incident waves as well as the heat transfer. In the case of bubble interaction, the attenuation coefficient first increases to its maximum value at the volume fraction of about 1% and then decreases. Fig. 2(b) describes the decreasing tendency of the sound speed in the bubbly liquid with the increase of the volume fraction. As shown in this figure, the decrease of the sound speed becomes slower at high volume fractions in the both cases. At a high volume fraction both the attenuation coefficient and the sound speed with bubble interaction is smaller than those without bubble interaction. Partly compared to the previously reported experimental data [26], these numerical results with bubble interactions show a better agreement than the results without bubble interactions. Thus, these simulation results with bubble interactions will be used in the following modeling of sound field distribution in a thin bubbly liquid.

Since high vibration amplitude is required during ultrasonic cavitation peening, in the following simulations, the vibration amplitude of 25 μm, 30 μm, 35 μm and 40 μm, which are corresponding to the driving current of 0.208 A, 0.250 A, 0.292 A and 0.333 A are investigated. Moreover, the vibration amplitude of the sonotrode is proportional to the driving current with a relationship of 120 μm/A [28]. The radius and the height of the calculated spatial volume are 5 mm and 8 mm, respectively. To obtain the sound field distribution, the integral in Eq. (11) has to be conducted at each point in the bubbly liquid.

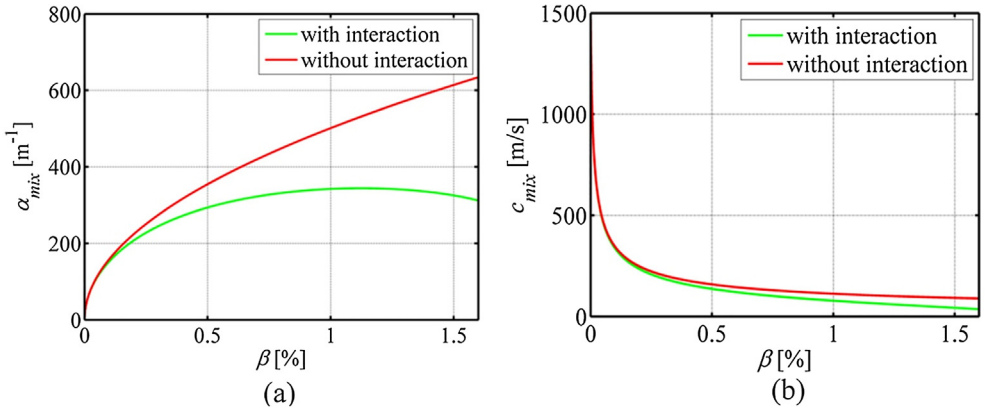


**Fig. 2.** Variation of attenuation coefficient (a) and sound speed (b) with the increase of vapor volume fraction.

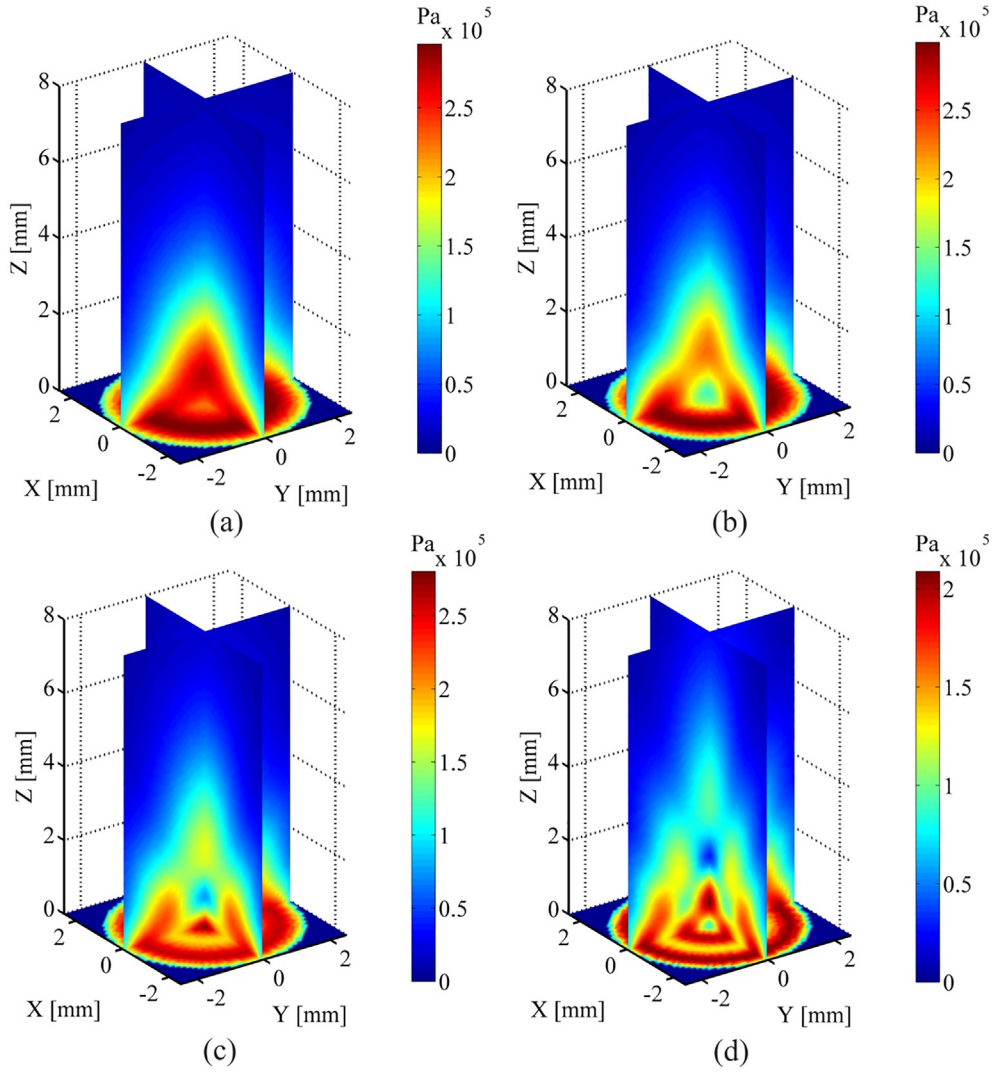


**Fig. 3.** Pressure fields for different driving currents at the resonance frequency of 23 kHz: (a) 0.208 A, (b) 0.250 A, (c) 0292 A and (d) 0.333 A.

In Fig. 3(a)–(d), the sound pressure at the driving currents of 0.208 A, 0.250 A, 0.292 A and 0.333 A are mapped, respectively. From the figures, some trends can be derived The highest sound pressure always occurs at the location close to the end of the sonotrode and the distribution is not uniform due to the sound near-field effects. With increasing the driving current, a very strong damping at the sound source is caused. This is due to the high bubble density caused by the high pressure value. As a result, the sound speed will decrease which has been shown in Fig. 2. Consequently, the sound pressure near the end of the sonotrode decreases although the vibration amplitude increases. The simulation distance is 8 mm. In this distance the sound pressure decreases gradually until it tends to vanish due to high attenuation. Thus, the simulation distance is enough for the following sound pressure analysis.

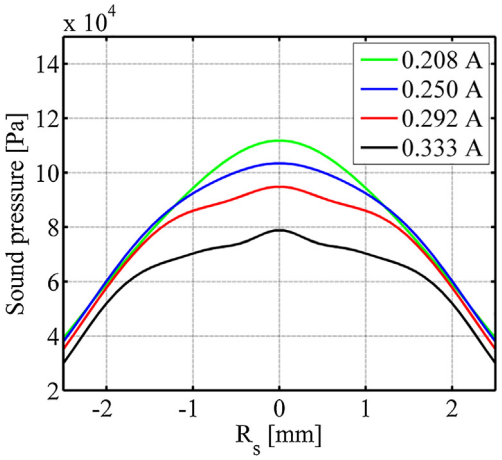


**Fig. 4.** The average sound pressure at different driving currents.

Owing to the circular symmetry, the pressure in the *XZ* plane can be used to infer the distribution of the sound pressure. As shown in Fig. 4, the average sound pressure distributions can in brief reflect the distribution of cavitation bubbles under different situations. The average pressure means the sum of the sound pressure values along *Z* direction are divided by the calculated number of the standoff distances. It can be seen that the average pressure at the center ($R_s = 0$) becomes smaller with increasing the driving current. A similar trend takes place at the edge of the sonotrode surface, but the change is much smaller. Therefore, the largest difference of the sound pressure distribution occurs at the central area of the calculated volume.

Using the boundary condition in Eqs. (12) and (13), the distribution of sound pressure in a small gap can be calculated after several overlapping as described in the theory section. Fig. 5 shows the distribution of sound pressure between the sonotrode and the workpiece at the standoff distance of 0.3 mm (top), 0.7 mm (middle) and 1.3 mm (bottom) and at the driving current of 0.333 A. The figure shows that the highest sound pressure occurs at the central regions on the sonotrode tip and the workpiece surface. The strongest cavitation intensity is also expected to be generated at the central area of the treatment surface. Nevertheless, the distribution of sound pressure at the standoff distance of 0.3 mm is more even than that at the other standoff distances. At this standoff distance, the growths and the collapses of the cavitation bubbles are affected by the small gap, which leads to the relative small impacts on the workpiece surface. When the standoff distance increases to 0.7 mm, the sound pressure on the workpiece decreases and the distribution of the sound pressure becomes uneven, but the impacts are expected to be the largest. It is because there is no gap limitation and the energy loss is less compared to that at the standoff distance of 1.3 mm. Thus, the standoff distance of around 0.7 mm is considered as the optimal standoff distance. This was validated in the previous study of ultrasonic cavitation peening [28], in which the most severe erosion occurs at the central area and at the standoff distance of about 0.7 mm. From these figures, the distribution of sound pressure on the workpiece surface can be directly obtained instead of the further calculations. The distributions will be analyzed in the following sections.

As described in this simulation section, the complex wave number with the consideration of bubble interactions is used in the calculation of sound field. Then, the sound field with and without boundaries is obtained. The simulation results will be validated in the following SCL experiments.

## 4. Experimental setup and methods

Fig. 6 shows the experimental setup for the investigation of cavitation bubbles in small gaps. The sonotrode was partly immersed in the reaction solution. The distance between the solution surface and the sonotrode tip was always kept at 10 mm. The diameter of the tip end is

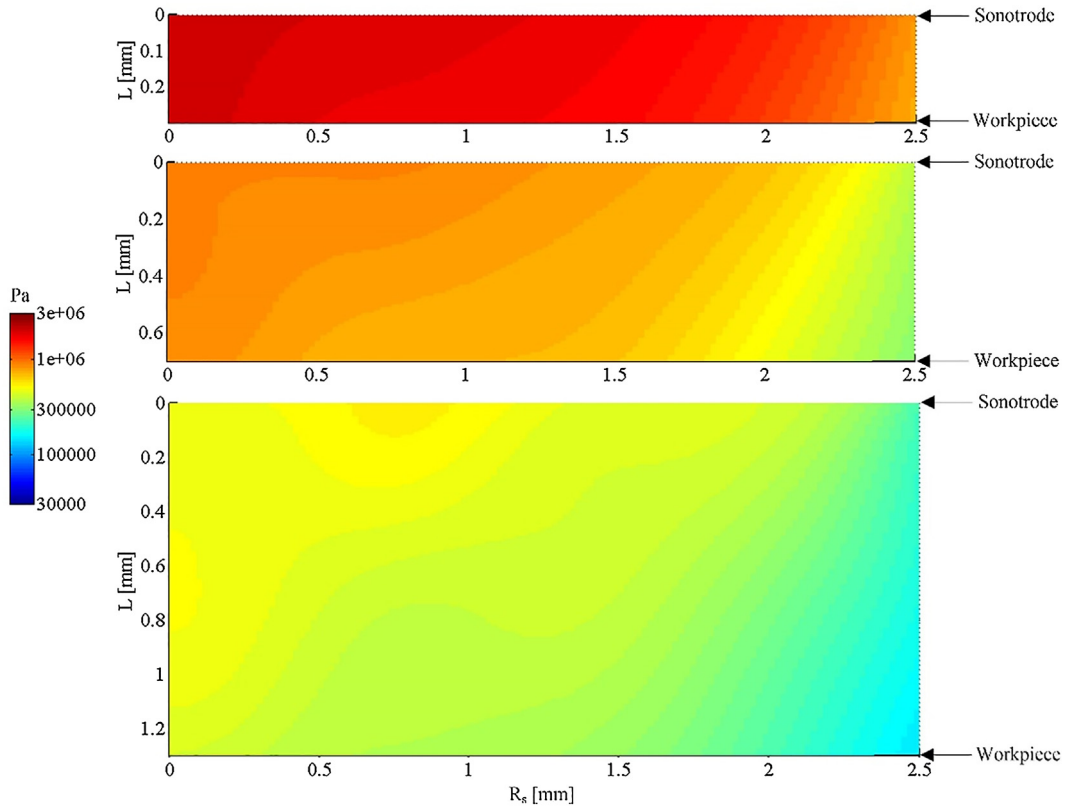


**Fig. 5.** The distribution of sound pressure in different gaps at the driving current of 0.333 A.

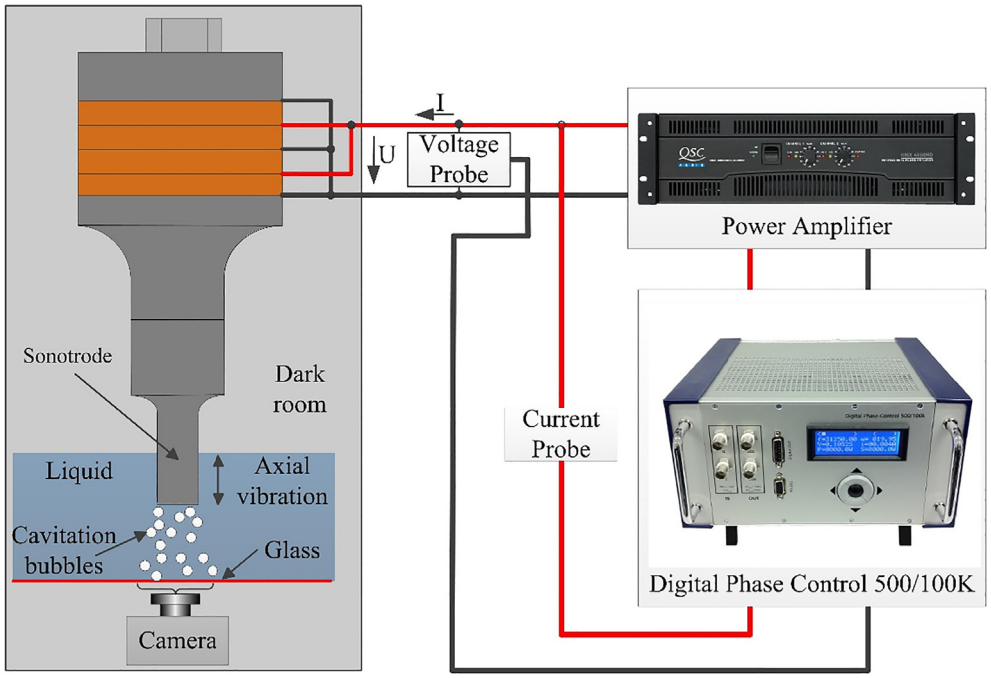


**Fig. 6.** The SCL experimental setup.

5 mm. A Nikon D3100 camera was set below the glass vessel to capture SCL images (f3.5-6.3, ISO400, focal length 262 mm and exposure time 90 s). The transducer used here is a classical sandwich transducer and ran at its first longitudinal resonance frequency at ~23 kHz. The transducer was driven at resonance by a digital phase control unit (IDS Digital-Phase Control 500/100 k) [27] with a power amplifier QSC 4050. The variations of the standoff distances are adjusted and confirmed by a displacement sensor (Solartron LVDT AS/150). In resonance, the vibration displacement amplitude $\hat{X}$ is proportional to the current amplitude $\hat{I}$ [28]. A current probe (Tektronix P6021) was used to measure the current values.

The solution used in the experiments consisted of luminol ($C_8H_7N_3O_2$) (0.004 mol/L), NaOH (0.1 mol/L) and pure water. The standoff distance was varied between 0.1 mm and 1.3 mm with the interval of 0.1 mm. Different driving currents 0.125 A, 0.208 A, 0.250 A, 0.292 A and 0.333 A were applied. At each standoff distance and with each driving current, five photos were taken corresponding to different driving currents. All of the experiments were carried out in a dark room.

## 5. Experimental results and discussion

In this section, the simulation results and the experimental results will be compared and analyzed. In order to minimize the distraction of the background light, the relative light intensity which is the difference between the original light intensity and the background light intensity was used. According to the previous investigation [30], the energy of the light radiated is proportional to the energy stored in a bubble. Therefore, with the same initial bubble size, the larger the maximum diameter of the bubble, the stronger the light intensity. The maximum bubble size depends on the sound pressure. Thus, the distribution of sound pressure can be identified by the SCL relative intensity. The mean values of the SCL relative intensities are shown in Fig. 7.

When the driving current is 0.125 A, the SCL relative intensity fluctuates in the range of 1 and 6. The value of the SCL relative intensity at this low driving current is smaller than that at other high driving currents, since low driving current does not have enough energy to generate strong cavitation. Thus, at the driving current of 0.125 A, the SCL relative intensity is weak and less influenced by the variation of the

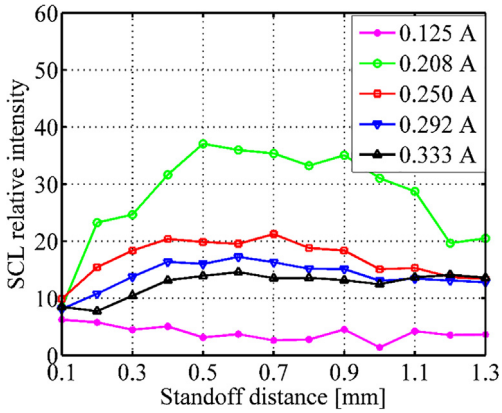


**Fig. 7.** Mean light intensity distribution at different standoff distances and driving currents.

standoff distance.

The values of SCL relative intensity at the standoff distance of 0.1 mm are nearly the same for the driving currents of 0.208 A, 0.250 A, 0.292 A and 0.333 A. With the increase of the standoff distance, the values of SCL relative intensity increase while a lower driving current exhibits higher values. This is because that the growth and collapses of the cavitation bubbles are limited by the small gap, the cavitation intensity does not increase even when the input energy becomes higher. When the driving current increases, both of the sound pressure and the speed decrease, but the decrease rate of the sound speed is quicker, which leads to the generation of more cavitation bubbles with smaller sizes. As a result, both of the concentration of the luminol in the solution and the cavitation intensity of the single bubble decrease. Thus, the values of the SCL relative intensity get weaker.

With the increase of the standoff distance, the dynamics of cavitation bubbles is not limited while much energy is emitted. When the standoff distance increases continuously, many cavitation bubbles exist in the gap. The cavitation intensity at the bottom of the glass is weaker than that near the transducer surface. The light caused by SCL is reflected, scattered and absorbed by the bubble layer near the surface of

the glass. As a result, the SCL relative intensity decreases again as the light of SCL is weakened when it travels through the cavitation bubble layers.

Under our experimental conditions, the mean SCL relative intensities with different driving currents have the similar tendency along with increasing the standoff distance. The strongest cavitation occurs at the range of a standoff distance between 0.5 mm and 0.7 mm, since there is less attenuation and less limitation of rigid walls. The change of the mean SCL relative intensity at different driving current is also similar to the change of average sound pressure as shown in Fig. 4. Therefore, this range can be considered as the optimal treatment standoff distance during ultrasonic cavitation peening. Compared to the peening results by ultrasonic cavitation in the previous investigation [28], there are the similar tendencies at different driving current. However, the results from the SCL experiments should be more precise, since there are almost changes of the topographies during cavitation process due to the strong corrosion resistance of the glass bottom. Therefore, the distribution of the cavitation bubble in the small gaps is not affected by the change of the workpiece surface topographies.

The mean distributions of cavitation bubbles at different conditions have been introduced above. However, the local distributions of cavitation bubbles are still essential to investigate, since the near sound field results in different treatment surface properties on a same workpiece after ultrasonic cavitation peening process. The local distribution of the cavitation in small gaps is further studied by analyzing the case at the driving current of 0.208 A and the standoff distance of 0.7 mm. In order to obtain better results, the photos were rotated every 45 degree and then the average values were calculated. As shown in Fig. 8(a) the light intensity is the highest at the centre area. There is a ring area where the cavitation intensity is higher comparing to other areas except the centre area. The values of the SCL relative intensity along the diameter is plotted in Fig. 8(b).

Following the above process method, the SCL relative intensities at the driving current of 0.208 A, 0.250 A, 0.292 A and 0.333 A are shown in Fig. 9. The strongest SCL relative intensity always occurs at $R_s = 0$. It is found that at a low driving current, the SCL relative intensity is stronger than that at a high driving current. The reason has been introduced in the above explanation. Compared to the calculation results, there is a big difference at the standoff distances between 0.1 mm and 0.4 mm in the experiments. In the simulation results, the sound pressure becomes higher with reducing the standoff distance while for the experiments the cavitation intensity becomes lower along with decreasing the standoff distance due to the limitation of bubble growth and collapses.

From the above description, the effects of different standoff distances on the SCL relative intensity are clearly illustrated. However, the distributions of cavitation bubbles at a fixed standoff distance but different driving currents are still required for a complete understanding of the issue. In order to compare the calculation results and the simulation results on the workpiece surface. The sound pressure on the workpiece is calculated, since the main effect is caused by the cavitation bubbles near the treated surface. To show the change tendency at different driving current clearly, the driving current of 0.083 A, 0.125 A and 0.167 A are simulated additionally. The distribution of the sound pressure at the standoff distance of 0.3 mm, 0.7 mm and 1.3 mm are shown in Fig. 10(a), (b) and (c), respectively. The figures show that the strongest sound pressure distributes in the central area. The sound pressure in the central area increases first and then decreases with the increases of the driving current. It is because that the increase rate of the vibration amplitude is less than the decrease rate of the sound speed when the driving current is more than 0.208 A. It also can be seen that the distribution of the sound pressure become complicated with the increase of the driving current. This is because the number of the side lobes of the sound beam increases with the increase of the wave number. At the same driving current, the output power from the sonotrode is the same, but the energy density decreases with the increase the standoff distance. Therefore, the sound pressure decreases with the increase of the standoff distance.

Fig. 11(a)–(c) show the local distributions of SCL relative intensity corresponding to the conditions in Fig. 10(a)–(c), respectively. The primary variation tendency of the SCL relative intensity is similar to the corresponding variation of the sound pressure. The intensity of the SCL relative intensity decreases from $R_s = 0$, then a slightly increase occurs and finally decreases along with the increase of the $R_s$. The increase shows a ring area of SCL light when it is observed from the SCL photo. This is because the effects of the side lobes of the sound beam increase, which is shown in Fig. 5 as an example. However, the main lobe is still dominant, which leads to the strongest SCL relative intensity in the central region. Thus, during ultrasonic cavitation, ring erosion patterns on the treated workpiece surfaces would be produced. At the standoff distance of 0.7 mm, the ultrasonic cavitation peening process at different driving currents were carried out [9]. The erosion patterns on the workpiece surfaces are similar as the distribution of the cavitation bubbles which are captured by the SCL experiments.

From the comparison between the calculation results and the experimental results, it is found the highest sound pressure and the strongest cavitation intensity occur at $R_s = 0$. These studies can provide an estimation of the surface treatment effects for the ultrasonic cavitation peening.

## 6. Conclusion

In this paper, the sound field distribution model is improved with the consideration of bubble interactions. Then the SCL experiments were carried out to compare with the simulation results. In the simulation the sound speed and the attenuation coefficient are calculated with and without the bubble interactions. It is found that the sound speed with bubble interactions decreases more rapidly than that

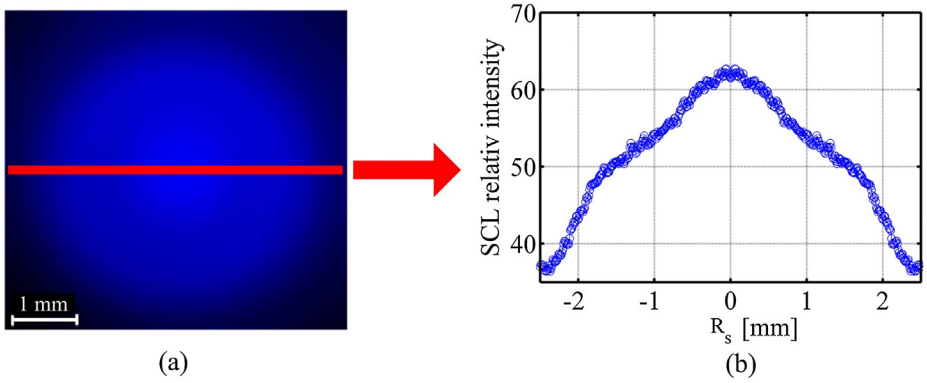


**Fig. 8.** Photo of SCL and light intensity distribution at the driving current of 0.208 A and the standoff distance of 0.7 mm.

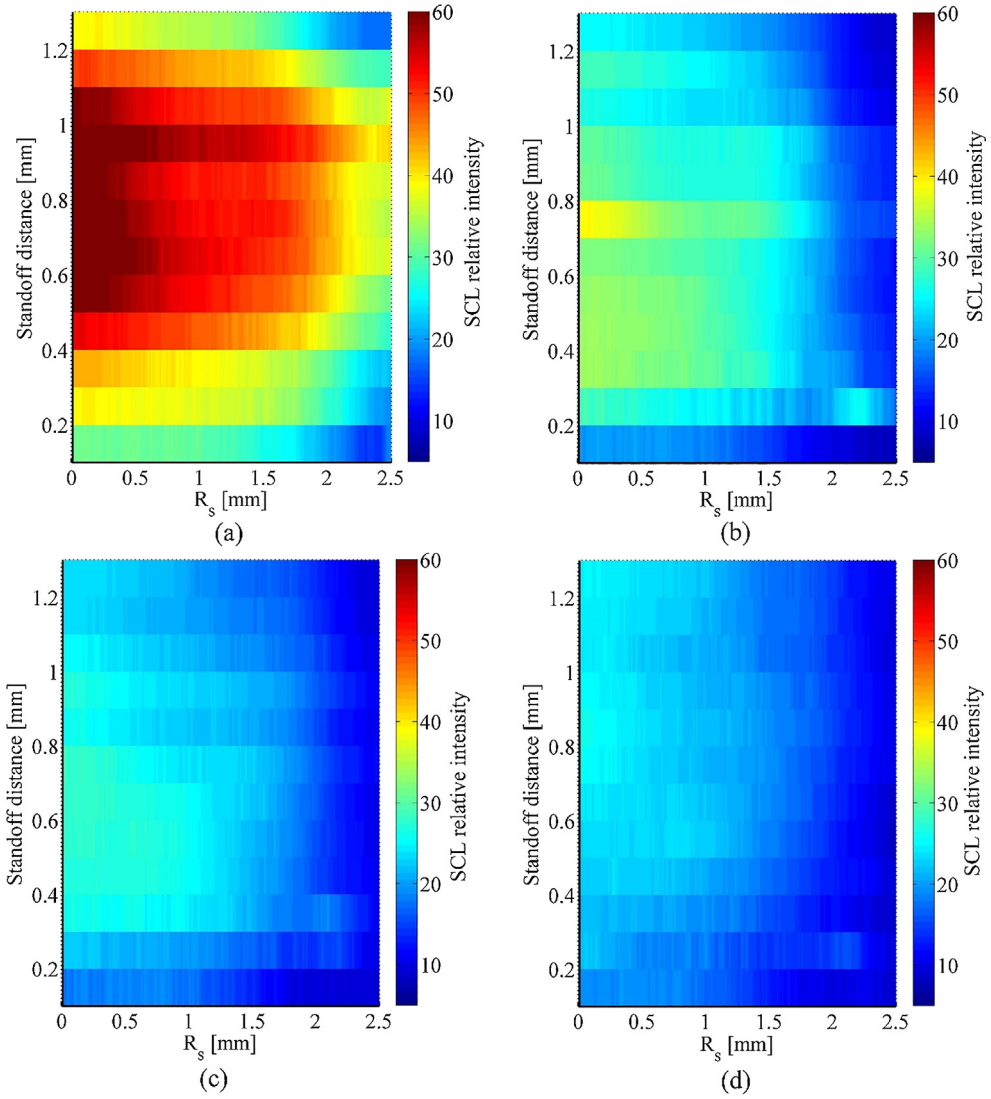


**Fig. 9.** SCL relative intensity distribution at driving currents of (a) 0.208 A, (b) 0.250 A, (c) 0.282 A and (d) 0.333 A.

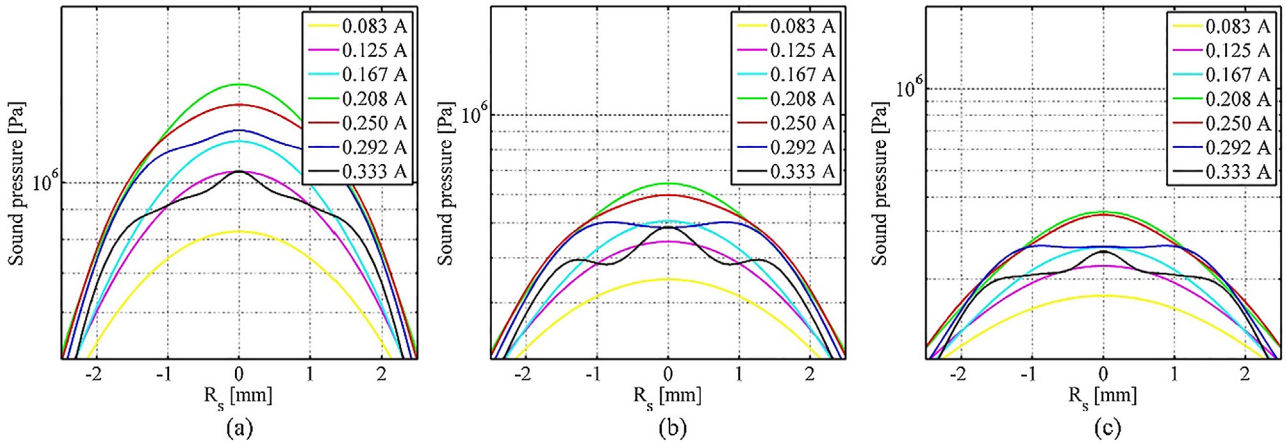


**Fig. 10.** The distribution of the local sound pressure distribution at standoff distances of (a) 0.3 mm, (b) 0.7 mm, (c) 1.3 mm.

without bubble interactions at the high volume fraction while the attenuation increases more slowly. As a result, the sound pressure first increases to a peak at the vibration amplitude of 25 μm and then decreases with increasing the vibration amplitude from 10 μm to 40 μm. Then the mean SCL relative intensity was investigated. The results show that the strongest SCL relative intensity occurs at the vibration amplitude of 25 μm. In the range of the vibration amplitude between 25 μm and 40 μm, the strongest cavitation intensity occurs at the standoff distances of 0.5–0.7 mm. For the local distribution of cavitation bubbles, the SCL experiments show that the strongest cavitation intensity

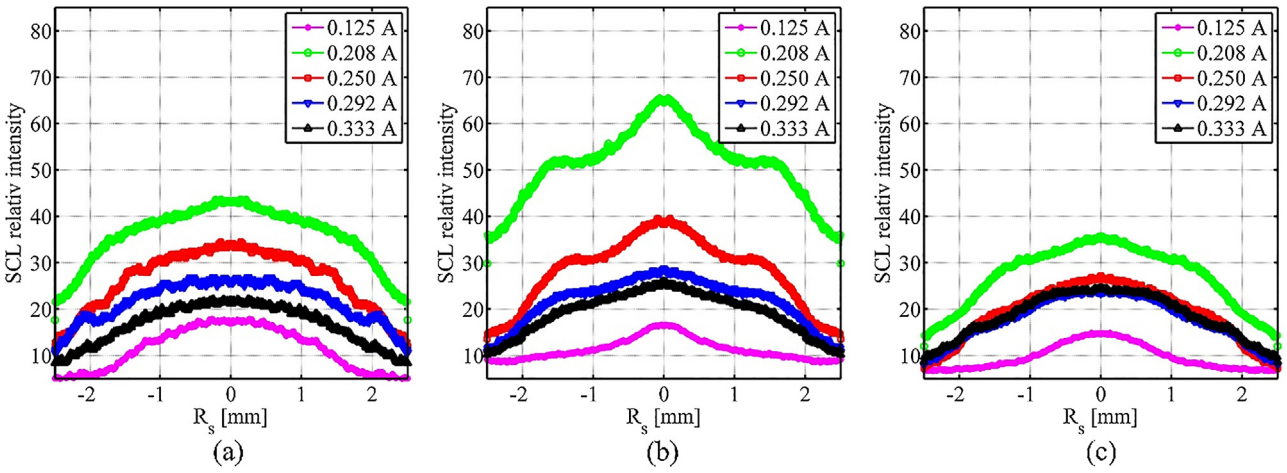


**Fig. 11.** The local distribution of SCL relative intensity at standoff distances of (a) 0.3 mm, (b) 0.7 mm, (c) 1.3 mm.

occurs at the center of the treated region, which can be validated by the previous investigations of ultrasonic cavitation peening. Compared to the calculation results, the big difference is at the range of standoff distance between 0.1 mm and 0.4 mm because of the limitation of the bubble growth and collapses. Due to the interactions of cavitation bubbles, the violent cavitation reaction always concentrates at the vicinity of $R_s$, which leads to the slightly difference from the simulation results as well. However, both the model and the SCL experiments verify the primary tendency of the cavitation intensity and distribution at the range of standoff distance between 0.5 mm and 1.3 mm, which can provide a guideline for the ultrasonic cavitation peening process.

## References


[1] K.H. Kim, G. Chahine, J.P. Franc, A. Karimi (Eds.), Advanced Experimental and Numerical Techniques for Cavitation Erosion Prediction, vol. 106, Springer, 2014.

[2] R. Ji, J. Jin, L. Wang, J. Zhang, A novel ultrasonic surface machining tool utilizing elastic traveling waves, Ultrasonics 80 (2017) 78–86, https://doi.org/10.1016/j.ultras.2017.05.001.

[3] D.G. Shchukin, E. Skorb, V. Belova, H. Möhwald, Ultrasonic cavitation at solid surfaces, Adv. Mater. 23 (17) (2011) 1922–1934, https://doi.org/10.1002/adma.201004494.

[4] M.R. Sriraman, R. Vasudevan, Influence of ultrasonic cavitation on surface residual stresses in AISI 304 stainless steel, J. Mater. Sci. 33 (1998) 2899–2904.

[5] M.R. Sriraman, R. Vasudevan, Influence of ultrasonic cavitation on surface residual stresses in AISI 304 stainless steel, J. Mater. Sci. 33 (11) (1998) 2899–2904, https://doi.org/10.1023/A:1017506424360.

[6] Y. Gao, B. Wu, Z. Liu, Y. Zhou, N. Shen, H. Ding, Ultrasonic cavitation peening of stainless steel and nickel alloy, J. Manuf. Sci. Eng. 136 (1) (2014) 014502, https://doi.org/10.1115/1.4025756.

[7] T. Sasaki, S. Hasegawa, M. Nakagawa, S. Yoshida, Water cavitation peening by ultrasonic vibration for improvement of fatigue strength of stainless steel sheet, Residual Stress, Thermomechanics & Infrared Imaging, Hybrid Techniques and Inverse Problems, Springer, Cham, 2014, pp. 221–227 https://doi.org/10.1007/978-3-319-00876-9_27.

[8] S.J. Kim, J.Y. Jeong, S.J. Lee, Effects of temperature and amplitude on damage behavior of Al alloy by ultrasonic vibration cavitation, Sci. Adv. Mater. 6 (10) (2014) 2185–2190, https://doi.org/10.1166/sam.2014.2064.

[9] F. Bai, K.A. Saalbach, L. Wang, X. Wang, J. Twiefel, Impact of time on ultrasonic cavitation peening via detection of surface plastic deformation, Ultrasonics 84 (2018) 350–355, https://doi.org/10.1016/j.ultras.2017.12.001.

[10] H. Seki, K. Fujita, T. Ogasawara, H. Takahira, Numerical simulations of growth and collapse of a bubble between two parallel walls, in: ASME/JSME/KSME 2015 Joint Fluids Engineering Conference, American Society of Mechanical Engineers, 2015, July, pp. V02AT05A004–V02AT05A004.

[11] T. Ogasawara, N. Tsubota, H. Seki, Y. Shigaki, H. Takahira, Experimental and numerical investigations of the bubble collapse at the center between rigid walls, in: Journal of Physics: Conference Series, vol. 656, No. 1, IOP Publishing, 2015, p. 012031. https://doi.org/10.1088/1742-6596/656/1/012031.

[12] V.V. Kucherenko, V.V. Shamko, Dynamics of electric-explosion cavities between two solid parallel walls, J. Appl. Mech. Tech. Phys. 27 (1) (1986) 112–115, https://doi.org/10.1007/BF00911130.

[13] A. Abouel-Kasem, S.M. Ahmed, Bubble structures between two walls in ultrasonic cavitation erosion, J. Tribol. 134 (2) (2012) 021702, https://doi.org/10.1115/1.4005217.

[14] M. Lee, J. Oh, Synergistic effect of hydrogen peroxide production and sonochemiluminescence under dual frequency ultrasound irradiation, Ultrasonics Sonochem. 18 (3) (2011) 781–788, https://doi.org/10.1016/j.ultsonch.2010.11.022.

[15] G.J. Price, N.K. Harris, A.J. Stewart, Direct observation of cavitation fields at 23 and 515 kHz, Ultrasonics Sonochem. 17 (1) (2010) 30–33, https://doi.org/10.1016/j.ultsonch.2009.04.009.

[16] Z. Wei, J.A. Kosterman, R. Xiao, G.Y. Pee, M. Cai, L.K. Weavers, Designing and characterizing a multi-stepped ultrasonic horn for enhanced sonochemical performance, Ultrasonics Sonochem. 27 (2015) 325–333, https://doi.org/10.1016/j.ultsonch.2015.05.013.

[17] K. Yasuda, T. Torii, K. Yasui, Y. Iida, T. Tuziuti, M. Nakamura, Y. Asakura, Enhancement of sonochemical reaction of terephthalate ion by superposition of ultrasonic fields of various frequencies, Ultrasonics Sonochem. 14 (6) (2007) 699–704, https://doi.org/10.1016/j.ultsonch.2006.12.013.

[18] T. Suzuki, K. Yasui, K. Yasuda, Y. Iida, T. Tuziuti, T. Torii, M. Nakamura, Effect of dual frequency on sonochemical reaction rates, Res. Chem. Intermed. 30 (7–8) (2004) 703–711, https://doi.org/10.1163/1568567041856873.

[19] M. Ashokkumar, F. Grieser, The effect of surface active solutes on bubbles in an acoustic field, Phys. Chem. Chem. Phys. 9 (42) (2007) 5631–5643, https://doi.org/10.1039/B707306M.

[20] K.W. Commander, A. Prosperetti, Linear pressure waves in bubbly liquids: comparison between theory and experiments, J. Acoust. Soc. Am. 85 (2) (1989) 732–746, https://doi.org/10.1121/1.397599.

[21] L. Van Wijngaarden, On the equations of motion for mixtures of liquid and gas bubbles, J. Fluid Mech. 33 (3) (1968) 465–474, https://doi.org/10.1017/S002211206800145X.

[22] S. Dähnke, Modellierung sonochemischer Prozesse: Berechnung von Schallfeldern und Kavitationsblasenverteilungen, 1999.

[23] D. Fuster, J.M. Conoir, T. Colonius, Effect of direct bubble-bubble interactions on linear-wave propagation in bubbly liquids, Phys. Rev. E 90 (6) (2014) 063010, https://doi.org/10.1103/PhysRevE.90.063010.

[24] S.W. Dahnke, F.J. Keil, Modeling of linear pressure fields in sonochemical reactors considering an inhomogeneous density distribution of cavitation bubbles, Chem. Eng. Sci. 54 (13–14) (1999) 2865–2872, https://doi.org/10.1016/S0009-2509(98)00340-6.

[25] S. Dähnke, F.J. Keil, Modeling of three-dimensional linear pressure fields in sonochemical reactors with homogeneous and inhomogeneous density distributions of cavitation bubbles, Indust. Eng. Chem. Res. 37 (3) (1998) 848–864, https://doi.org/10.1021/ie9703393.

[26] P.S. Wilson, R.A. Roy, W.M. Carey, Phase speed and attenuation in bubbly liquids inferred from impedance measurements near the individual bubble resonance frequency, J. Acoust. Soc. Am. 117 (4) (2005) 1895–1910, https://doi.org/10.1121/1.1859091.

[27] I. Ille, J. Twiefel, Model-based feedback control of an ultrasonic transducer for ultrasonic assisted turning using a novel digital controller, Phys. Proc. 70 (2015) 63–67, https://doi.org/10.1016/j.phpro.2015.08.043.

[28] F. Bai, K.A. Saalbach, Y. Long, J. Twiefel, J. Wallaschek, Capability evaluation of ultrasonic cavitation peening at different standoff distances, Ultrasonics 84 (2018) 38–44, https://doi.org/10.1016/j.ultras.2017.10.013.

[29] R. Jamshidi, B. Pohl, U.A. Peuker, G. Brenner, Numerical investigation of sonochemical reactors considering the effect of inhomogeneous bubble clouds on ultrasonic wave propagation, Chem. Eng. J. 189 (2012) 364–375, https://doi.org/10.1016/j.cej.2012.02.029.

[30] S.J. Putterman, K.R. Weninger, Sonoluminescence: how bubbles turn sound into light, Annu. Rev. Fluid Mech. 32 (1) (2000) 445–476.